Mechanics of cellular packing of nanorods with finite and non-uniform diameters

Mechanics of cellular packing of nanorods with finite and non-uniform diameters

Xin Yi[1,2,†], **Guijin Zou**[3] **and Huajian Gao**[3,*]

To understand the mechanics of cellular/intracellular packing of one-dimensional nanomaterials, we perform theoretical analysis and molecular dynamics simulations to investigate how the morphology and mechanical behaviors of a lipid vesicle are regulated by encapsulated rigid nanorods of finite and non-uniform diameters, including a cylindrical rod, a rod with widened ends, a cone-shaped rod and a screwdriver-shaped rod. As the rod length increases, the vesicle evolves from a sphere into different shapes, such as a lemon, a conga drum, a cherry, a bowling pin, or a tubular shape for long and thick rods. The contact between the vesicle protrusion and rod plays an important role in regulating the vesicle tubulation, membrane tension, and axial contact force on the rod. Our analysis provides a theoretical basis to understand a wide range of experiments on morphological transitions that occur in cellular packing of actin or microtubule bundles, mitotic cell division, and intracellular packing of carbon nanotubes.

1 Introduction

Understanding the biophysical mechanisms for cellular and intracellular packaging of one-dimensional materials is of fundamental importance for many cellular functions and biological processes, including cell shape control,[1–5] filopodial protrusion during cell movement,[6] mitotic cell division,[7–9] frustrated phagocytosis,[10] and cytotoxicity.[12] For example, long and stiff microtubule bundles within a vesicle could give rise to tubulation of the vesicle resembling the Greek letter ϕ with a pair of tubular membrane protrusions or a cherry-like shape with a single protrusion,[1–4] while encapsulated long flexible filaments become curved against the vesicle membrane and the vesicle adopts a non-axisymmetric dumpling-like shape.[13,14] Flexible ring-like filaments could fold into a (super-)coiled structure within a cell and lead to complex cell deformation.[4,5] Elongation of spindle microtubules within cell nucleus due to gene overexpression could result in abnormal tubulation of the nuclear envelope during mitosis.[7] Sister chromatids which become separated at the cell poles during anaphase are connected by thin microtubule bundles, and together form a dumbbell-like structure in the cell.[9]

In the field of pathogenicity, the need to assess the health safety of synthetic one-dimensional nanomaterials, such as carbon nanotubes, nanofibers, and asbestos, prior to widespread commercial use is calling for a systematic effort to understand the biophysical mechanisms of their interactions with cells and intracellular organelles following cell uptake.[10–12] Experimental results indicate that length[11] and elasticity[12] are important features that modulate the pathogenicity of encapsulated nanotubes. More specifically, long and stiff carbon nanotubes could induce lung injury, epithelioid granuloma, persistent interstitial inflammation and fibrosis, frustrated phagocytosis, and organelle damage.[10–12,15] Exposing the mesothelial lining of the chest cavity to long multiwalled carbon nanotubes induces asbestos-like and length-dependent pathogenic behaviors, including frustrated phagocytosis and giant cell formation.[10] Sufficiently long and stiff carbon nanotubes within lysosomes cause sustained tip contact with the inner lysosomal membrane, leading to lipid extraction, permeabilization, cathepsin B release into the cytoplasm, and eventually cell death, while biologically soft carbon nanotubes buckle within liposomes, consequently losing persistent tip contact and staying nonpathogenic.[12]

While a number of theoretical models have been established to understand and characterize the mechanical response of a vesicle to a confined rigid nanorod of different lengths,[1,3,12,16] two key parameters, nanorod diameter and shape, have been neglected in these previous studies where the vesicle was oversimplified as having point contact with a nanorod that exerts a pair of localized outward pushing forces upon the vesicle poles. Similar approaches have been employed in modeling the formation of tubular membrane protrusions induced by external forces[17–19] induced by, for example, cooperative movement of motor proteins[20,21] or optical/magnetic tweezers.[18]

In view of the accumulating experimental observations on cellular packing of nanorods with finite and non-uniform diameters, we aim to develop a more sophisticated theoretical model that explicitly accounts for contact between the membrane of a vesicle and side wall of an encapsulated nanorod, which allows us to handle more complex and general nanorod geometries under a wide range of membrane tension. Four different nanorod shapes are considered (Fig. 1): a cylindrical nanorod, a nanorod with two wide ends, a cone-shaped nanorod, and a screwdriver-shaped nanorod. Here the cylindrical nanorod serves as a representative for one-dimensional nanomaterials including (carbon) nanotubes, (gold) nanowires, (asbestos) nanofibers, micro-

[1]Department of Mechanics and Engineering Science, College of Engineering, Peking University, Beijing 100871, China. [2]Beijing Innovation Center for Engineering Science and Advanced Technology, Peking University, Beijing 100871, China. [†]E-mail: xyi@pku.edu.cn. [3]School of Engineering, Brown University, Providence, Rhode Island 02912, USA. [*]E-mail: huajian_gao@brown.edu

tubule bundles, and actin-based cellular protrusions of tubular shapes; the nanorod with two wide ends models dumbbell-like structures observed in mitotic cell division and engineered nanodumbbells used in biomedical imaging [22,23] and photodynamic therapy [24]; the cone-shaped nanorod could be used to depict carbon nanohorns which exhibit potential applications in drug delivery [25,26] and show low cytotoxicity at a low-uptake level [27] but at high doses induce lysosomal membrane permeabilization and subsequent release of lysosomal proteases, eventually leading to cell apoptosis; [28,29] the screwdriver-shaped nanorod of a sharp diameter variation can be viewed as a modified hybrid of the cylindrical nanorod and cone-shaped nanorod. To complement the theoretical analysis, molecular dynamics (MD) simulations are also performed to probe how the morphology and other mechanical behaviors of a vesicle are regulated by encapsulated rigid nanorods of different diameters and shapes. It will be shown that an initially spherical vesicle undergoes significant shape transformations that strongly depend on the nanorod length, shape, and diameter. Moreover, both the effective axial contact force on the nanorod exerted by the confining vesicle and the vesicle

membrane tension exhibit rich features of nonlinearity, non-monotonicity, and discontinuity. Our results shed light on the biophysical mechanisms for the cellular or intracellular packaging of microtubule bundles, mitotic cell division, as well as the pathogenicity of carbon nanotubes.

2 Model and methods

To analyze the response of an initially spherical vesicle of radius R to an encapsulated rigid nanorod of a finite diameter, we consider a theoretical model in which the deformed vesicle is of a fixed surface area $A(=4\pi R^2)$ at a pressure difference Δp with a protrusion induced by the nanorod with length $L \geq 2R$ (Fig. 1). In our analysis, the deformed vesicle is assumed to retain an axisymmetric configuration, which is confirmed by our MD simulations. The free energy of the system is described by the Helfrich functional [30]

$$E = \pi\kappa \int_0^l \left(\frac{\mathrm{d}\psi}{\mathrm{d}s} + \frac{\sin\psi}{r} \right)^2 r\mathrm{d}s - \Delta p(V - V_0),$$

where the first term is the elastic deformation energy of the vesicle with ψ, s, and κ being the tangent angle, arclength, and bending rigidity of the vesicle membrane, respectively; l denotes the undetermined total arclength of the vesicle; $V_0 = 4\pi R^3/3$ and $V = \pi \int_0^l r^2 \mathrm{d}s$ are the original and deformed volume of the vesicle under Δp. It is assumed that the membrane has no spontaneous curvature. The membrane deformation energy associated with the Gaussian modulus is constant due to the Gauss-Bonnet theorem and hence ignored here. In addition to the free energy of the system, there are two other key quantities characterizing the mechanical state of the vesicle: the effective membrane tension σ as a Lagrange multiplier conjugated to the fixed vesicle area A, and the effective axial contact force F between the nanorod and vesicle membrane, stretching the vesicle along the z-axis in our adopted cylindrical coordinate system.

As shown in Fig. 1, the two contact edges between the nanorod tips and membrane divide the vesicle into three portions, the top and bottom parts (thin red lines) and middle part (thick black lines). We employ the Monge parameterization based on the cubic B-spline curve approximation [19,31] to describe the profile of each part. For example, the profile of the bottom part is approximated as $z(r) = \sum b_i N_i(r)$ $(i = 0, \ldots, n)$, where b_i (control points) are the coefficients of the basis functions $N_i(r)$ defined recursively on a non-uniform knot vector of the variable r. A typical choice of the knot vector of a parameter $\eta \in [0, t]$ is described as $\{\eta_0, \ldots, \eta_{n+4}\}$ with $\eta_j = 0$ $(j = 0, \ldots, 3)$ and $\eta_j = t$ $(j = n+1, \ldots, n+4)$. Similar forms based on the cubic B-spline functions are employed for $r(z) = \sum c_i N_i(z)$ $(i = 0, \ldots, m)$ in the middle part and $z = z(r)$ in the top part. In the limiting case of a pair of localized point contact forces upon the vesicle poles, both the top and bottom parts vanish. Moreover, the parameterization transformations from $\psi(s)$ to $z(r)$ in the top and bottom parts and to $r(z)$ in the middle part are required to represent the
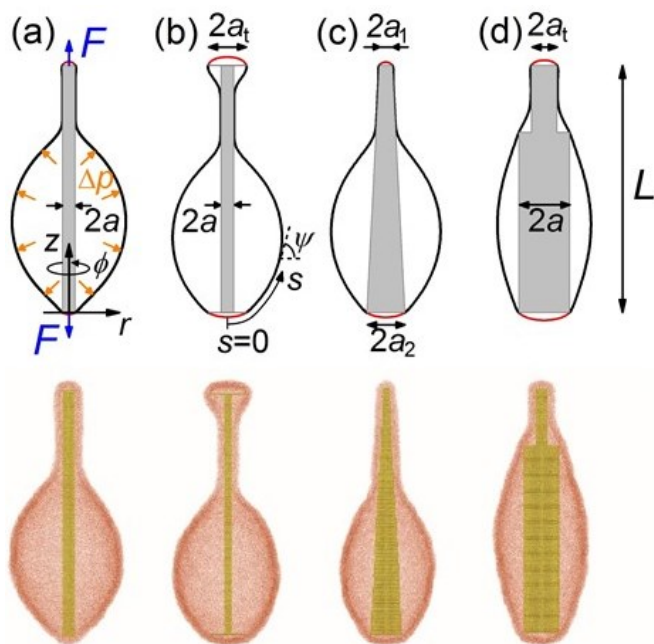

Fig. 1 Schematics and snapshots from MD simulations of the tubulation of a vesicle induced by an encapsulated rigid nanorod at a pressure difference Δp, (r, ϕ, z) being the adopted cylindrical coordinate system. The vesicle-nanorod morphologies for (a) a cylindrical nanorod of a uniform radius a, (b) a cylindrical nanorod with two widened tip ends of radii a_t, (c) a cone-shaped nanorod, and (d) a screwdriver-shaped nanorod. The encapsulated nanorod has length $L = 4R$. The two contact edges between the nanorod tips and the membrane divide the vesicle into three portions, the top and bottom parts (thin red lines) and middle part (thick black lines). Color settings of MD simulations throughout this work: beads of lipid molecules in orange and those modeling the nanorod in yellow.
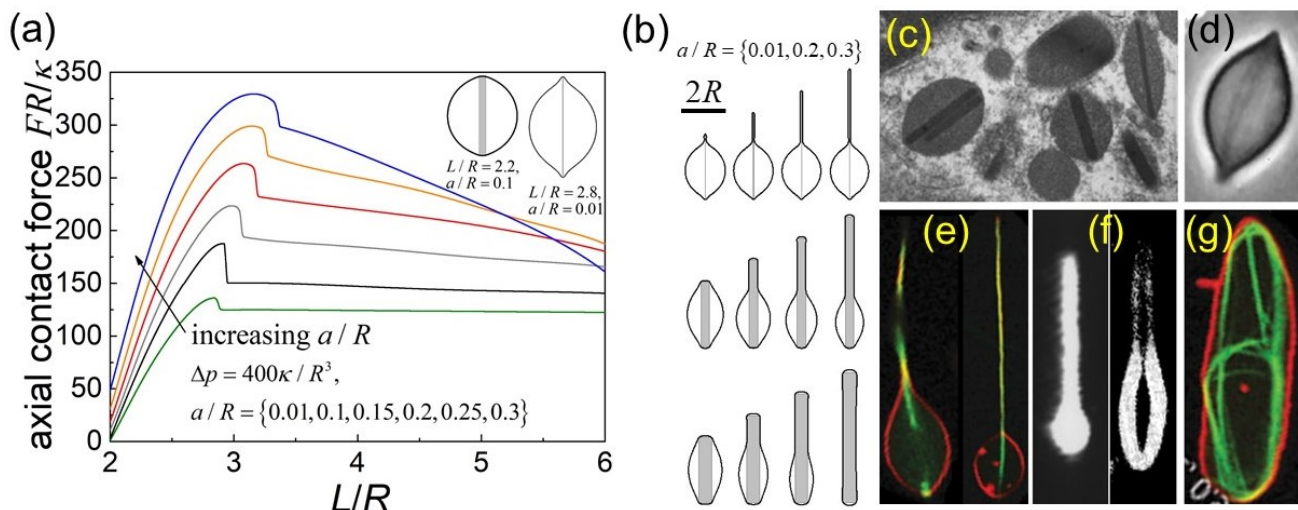
Fig. 2 (a) Normalized axial contact force FR/κ as a function of the normalized nanorod length L/R at $\Delta p = 400\kappa/R^3$ and different values of the normalized nanorod radius a/R. At extremely small a/R (e.g., $a/R = 0.01$), F saturates to a nearly constant value upon membrane protrusion formation. (b) Selected vesicle morphologies induced by the encapsulated rigid nanofiber of radius $a/R = 0.01, 0.2$, and 0.3, and length $L/R = 3, 4, 5$, and 6. The scale bar is of length $2R$. Inset in (a) showed the enlarged vesicle shape at $L/R = 2.2$, $a/R = 0.1$ and at $L/R = 2.8$, $a/R = 0.01$. (c-g) Experimental images of the observed vesicle morphologies induced by one-dimensional nanomaterials of different radii, lengths, and structures. (c) Lysosomes containing stiff single-walled carbon nanotubes in a cell from the mice ileum. Reprinted with permission from ref. 43. Copyright 2010, Elsevier, Ltd. (d) A lemon-shaped vesicle with a pair of protruding tips. Reprinted with permission from ref. 3. Copyright 1998, the American Physical Society. (e) Cherry-shaped vesicles, each with a single tubular membrane protrusion enclosing a stiff long microtubule. (f) A vesicle encapsulating a thick nanorod exhibiting a bowling pin-like shape. Left subfigure is reprinted with permission from ref. 1. Copyright 1998, the Physical Society of Japan. Right subfigure is reprinted with permission from ref. 2. Copyright 1998, Elsevier, Ltd. (g) A vesicle containing a cage-shaped actin network exhibits a thick, rod-like shape. Both (e) and (g) are reprinted with permission from ref. 4. Copyright 2015, the Royal Society of Chemistry.

free energy E in cylindrical coordinates. With the geometric relations $dr/ds = \cos\psi$ and $dz/ds = \sin\psi$, the radial and azimuthal principal curvatures for the top and bottom parts are $d\psi/ds = z''(1 + z'^2)^{-3/2}$ and $r^{-1}\sin\psi = r^{-1}z'(1 + z'^2)^{-1/2}$, respectively, with $z' \equiv dz/dr$ and $z'' \equiv d^2z/dr^2$. The radial and azimuthal principal curvatures in the middle part are $d\psi/ds = -r''(1 + r'^2)^{-3/2}$ and $r^{-1}\sin\psi = r^{-1}(1 + r'^2)^{-1/2}$, respectively, with $r' \equiv dr/dz$ and $r'' \equiv d^2r/dz^2$.

The minimum energy state of the vesicle at each given L is numerically determined through the interior-point method in constrained nonlinear optimization,[32] in which the fixed surface area A serves as an equality constraint, and inequality constraints are introduced to prevent penetration between the membrane and encapsulated nanorod. In the case of a straight, cylindrical nanorod with a uniform radius a (Fig. 1a), we have the boundary condition $\psi = 0$ at the south pole ($s = 0$) of the vesicle requiring $b_0 = b_1$, and continuities of the r coordinate and tangent angle ψ at the lower contact edge ($z = 0$) requiring $c_0 = a$ and $9(c_1 - a)z_n = (r_n - a)z_4$. Here, r_n represents the $(n+1)$th component in the knot vector of r in the bottom part, and z_n is the $(n+1)$th component in the knot vector of z in the middle part. Other boundary conditions include $\psi = \pi$ at the north pole ($s = l$) of the vesicle and continuities of r and ψ at the upper contact edge ($z = L$). The nanorods of other shapes, as shown in Fig. 1b-e, require different forms of boundary conditions at the contact edges, which could be determined in a similar manner as discussed above. Once the

state of the minimum energy E is obtained, the corresponding vesicle shape and effective membrane tension σ as a Lagrange multiplier are known. The effective axial contact force F as a conformational force arising from the vesicle deformation is determined numerically from $F = dE/dL$.

In addition to the theoretical analysis, coarse-grained MD simulations are performed to demonstrate the roles of nanorod size and shape on the vesicle-nanorod interaction. Both the solvent-free modeling[14,33–35] and dissipative particle dynamics simulations[19,36–39] has been demonstrated to be effective and efficient in studying the mechanical behaviors of biomembranes. In our simulation setup, the lipid bilayer of the vesicle is composed of solvent-free lipid molecules. Each lipid molecule is modeled as three connected beads, one bead representing the hydrophilic head and the other two the hydrophobic tail. The pressure difference across the lipid membrane is maintained by imposing outward forces on the lipid heads along the director of the lipid molecules. The encapsulated nanorod consists of a single wall of folded two-dimensional triangular lattices. Other details of the simulations, such as the nanorod geometries (Fig. S1a), simulation procedures, calculations of the axial contact force, and interaction potentials,[33,34] can be found in the supplementary information (SI). To reduce the computational cost, the vesicle in our MD simulations is chosen initially as a sphere of radius $R = 50$ nm, consisting of around 5×10^4 lipid molecules. The bending rigidity κ of this model membrane is about 12 k_BT deter-
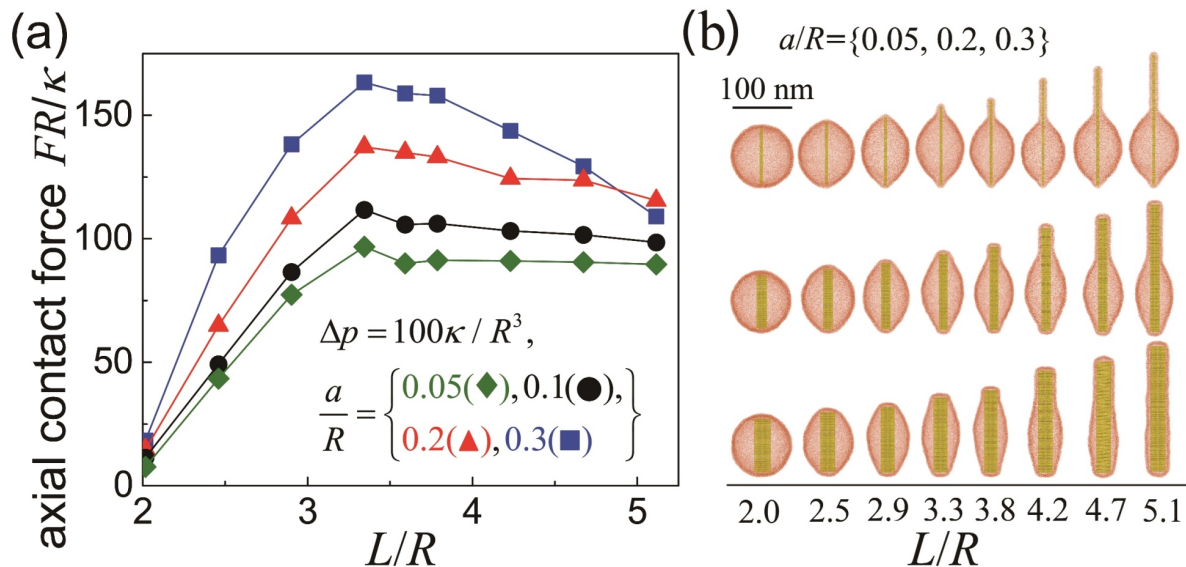
Fig. 3 (a) Axial contact force and (b) vesicle morphology induced by a nanorod of length L and radius a, as determined from MD simulations.

mined by the adopted interaction potentials.[35] The lateral dimensions of the simulation box are $160\,\text{nm} \times 160\,\text{nm}$. To avoid membrane rupture due to membrane tension while still capturing the mechanical interplay between the nanorod and vesicle, the outward forces are taken as 1.95×10^{-3} kcal·mol^{-1}·nm^{-1} on each lipid of area $0.68\,\text{nm}^2$ in our CG model, which corresponds to a pressure difference Δp around 40 kPa or a dimensionless pressure of $\Delta p R^3 / \kappa = 100$, as opposed to $\Delta p R^3 / \kappa = 400$ assumed in our theoretical analysis. The canonical (NVT) ensemble is used in the simulations which are performed based on LAMMPS[40] at a constant temperature of 310 K under the Nose-Hoover thermostat.[41,42] We focus on the equilibrium morphology and axial contact force of the vesicle-nanorod system.

3 Results

We first investigate the case of a vesicle containing a straight, rigid, cylindrical rod of length $L/R \geq 2$ and uniform radius a. Fig. 2a shows that the effective axial contact force F first increases almost linearly with the nanorod length L, rises to a peak value and then decreases upon the formation of a tubular membrane protrusion. Similar profiles are observed for the effective membrane tension σ (Fig. S2). Note that the peak values of F and σ are not located at the same value of L/R at given Δp. The force variation is accompanied by a transformation of the vesicle shape (Fig. 2b). At extremely small a/R (e.g., $a/R = 0.01$), curves of F and σ exhibit indistinguishable differences from those due to a pair of point forces on the vesicle poles, as expected, and the vesicle transforms from an initial sphere to a lemon-like shape with a pair of protruding tips, and to a cherry-like shape with a thin, long tubular membrane protrusion and a relatively large bulge (Fig. 2b). As a/R increases, the sizes of the two protruding tips and the tubular

protrusion increase, the lemon-like shape gradually becomes a conga drum-like shape, and the cherry-like shape becomes a bowling pin-like shape with a tubular membrane protrusion with radial size comparable to that of the bulge. For large a/R and L/R (e.g., $a/R = 0.3$ and $L/R = 6$), the vesicle exhibits a rod-like shape enclosing the nanorod (Fig. 2b). Due to the finite size of the nanorod, the vesicle is deformed at $L/R = 2$ with non-zero axial contact force F (Fig. 2a). The profiles of the normalized axial contact force and membrane tension at $\Delta p R^3 / \kappa = 200$ (see Fig. S3) exhibit similar trends to these at $\Delta p R^3 / \kappa = 400$ (Figs. 2a and S2).

To validate the theoretical analysis, we simulate vesicles with encapsulating nanorods of different radii and lengths (Fig. 3a). The simulations yield force profiles and vesicle morphologies similar to those from the theoretical analysis shown in Fig. 2. The effective axial contact force F, as the total vertical elastic force applied by the deformed vesicle, rises to a peak value at a certain L/R and then decreases upon the formation of a tubular membrane protrusion. As the rod radius a/R increases, F also increases, until the vesicle becomes rod-shaped at sufficiently large L/R (Fig. 3b).

In the absence of a pressure difference, there is no membrane protrusion or sharp transformation of the vesicle shape; F and σ increase smoothly and monotonically with L/R (Fig. S4). As L increases, the vesicle becomes thinner while retaining a rod-like shape. Once contact between the rod wall and vesicle membrane is established, F and σ increase at a much higher rate, as shown in Fig. S4 in the case of $a/R = 0.3$ and L/R beyond a value of approximately 5.5.

The theoretically predicted morphologies of vesicles containing nanorods of different sizes are consistent with experimental observations for a wide range of cell activities. In treating Alzheimer disease, single-walled carbon nanotubes (SWCNTs) with precisely controlled doses preferentially en-
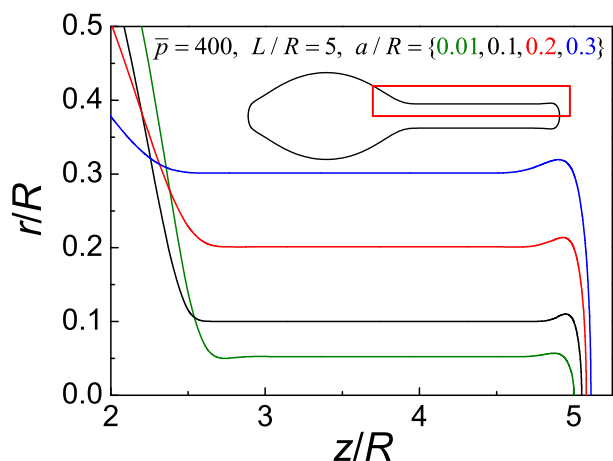
Fig. 4 Profile of a tubular membrane protrusion magnified in the radial direction for $L/R = 5$. Inset: vesicle morphology induced by the encapsulated nanofiber of radius $a = 0.2R$ and length $L = 5R$. The red curve corresponds to the zoomed-in vesicle portion in the red rectangle. The nanotube is not shown here for clarity.

ter lysosomes as pharmacological targets in neurons and neurites, and serve as drug carriers to deliver preloaded acetylcholine.[43] It is demonstrated that lysosomes containing SWCNTs of intermediate lengths exhibit lemon-like shapes, as shown in Fig. 2c,[43] though the mechanisms responsible for a SWCNT-based neuroprotective approach for Alzheimer disease remain elusive.[43,44] Lemon-shaped vesicles with a pair of more evident protruding tips are observed as the microtubule polymerizes within a phospholipid vesicle (Fig. 2d).[3] Our theoretical analysis indicates that a vesicle containing a stiff, thin, long nanorod exhibits a cherry-like shape, or a bowling pin-like shape for a thick, long nanorod. As shown in Fig. 2e, liposomes encapsulating thin, long actin-fascin bundles do exhibit cherry-like shapes,[4] and liposomes encapsulating long, thick microtubule bundles of different L/R exhibit bowling pin-like shapes (Fig. 2f).[1,2] In the case of a cage-shaped actin network, which can be approximated as a thick rod (Fig. 2g), the confining liposome exhibits a rod-like shape. These experimental observations are all consistent with our theoretical results and MD simulations.

Fig. 4 shows that the tip region of a tubular membrane protrusion exhibits a slightly larger radius than that of the cylindrical region of the protrusion, while the base region connecting the vesicle bulge exhibits either slight constriction when there is no contact between the encapsulated nanorod and vesicle membrane (e.g., the case of $a/R = 0.01$ in Fig. 4) or smooth contact with the nanorod wall (e.g., cases of $a/R = 0.1, 0.2$, and 0.3 in Fig. 4). Previous theoretical studies indicate that the shape of the protrusion tip is governed by a fourth-order linear differential equation and can be characterized by a sum of sinusoids with exponentially damped amplitudes.[45–47] As a increases, the tip region affected by the exponentially decaying oscillations expands.

To investigate whether and how the nanorod tip size affects

the morphology of a confining vesicle, we perform a number of case studies with both theoretical analysis and MD simulations on the interaction between the vesicle and an encapsulated nanorod with two widened tips, as shown in the inset in Fig. 5. In our theoretical analysis, the tip thickness is assumed to be negligible, and in the MD simulations, the tip contains only one layer of coarse-grained beads. Fig. 5 shows that the axial contact force F increases as the tip radius a_t increases before the formation of the tubular protrusion and then levels off to a constant. The membrane tension σ first increases and gradually rises to a maximum. Upon vesicle tubulation and with increasing contact between the vesicle membrane and nanorod wall, the membrane tension decreases linearly with respect to L/R (Fig. S5a). More vesicle morphologies from the MD simulations can be found in Fig. S5b. The nanorod with a wider tip requires a larger length L to overcome a larger axial contact force F for vesicle tubulation. The rising portions of the force curves for $a_t/R = 0.1, 0.2$, and 0.3 in Fig. 5 overlap those for $a/R = 0.1, 0.2$, and 0.3 in Fig. 2. This is because the vesicle before tubulation has no contact with the rod wall and only senses the tip size of the nanorod in the pretubulation stage. A key feature of Fig. 5 is that the peak force is proportional to the size of the nanorod tip. A similar size-dependent feature has been observed in membrane protrusions induced by an external pulling force, which is found to be proportional to the size of the region on which it is exerted.[18,19,48]

In Figs. 2 and 3, the nanorods under consideration have uniform diameters. To investigate the effects of non-uniform cross-section of an encapsulated nanorod, we consider vesicle tubulation induced by cone- and screwdriver-shaped nanorods and determine the associated F and σ. As shown in Figs. 6a and S6a for cone-shaped nanorods, the axial contact force increases to a peak value followed by a drop upon vesicle tubulation, similar to the results in Figs. 2 and 5. It can be seen from Fig. 5 that the peak contact force is proportional to the size of the nanorod tip. Therefore, it is not surprising that vesicle tubulation occurs at the smaller end of the cone-shaped nanorod and at a smaller value of L/R compared to that in the case of a cylindrical nanorod. As shown in Fig. 6a, for a truncated cone of $a_1/R = 0.1$ and $a_2/R = 0.3$, the peak value of F is located around $L/R = 2.6$, which is smaller than the values of 2.9 or 3.2 for a uniform nanorod with $a_1/R = 0.1$ or 0.3 in Fig. 2. A similar conclusion is obtained at $a_2/R = 0.1$ and $a_2/R = 0.2$. Although the peak force was not captured by our MD simulations due to the narrow range of parameter values within which it is located, as shown in Fig. 6a, we could observe similar behaviors from the simulated equilibrium morphologies. For example, the vesicle encapsulating a truncated cone of $a_1/R = 0.1$ and $a_2/R = 0.3$ forms a tubular membrane protrusion around $L/R = 3.3$, as shown in Fig. S6b; in contrast, it retains a lemon-like shape without tubular protrusions when encapsulating a uniform nanorod of the same L/R (Figs. 3 and S9b). Moreover, the peak force in Fig. 6a is slightly higher than the peak force in Fig. 2. A similar behavior is observed from MD simulations (comparing Fig. S6a
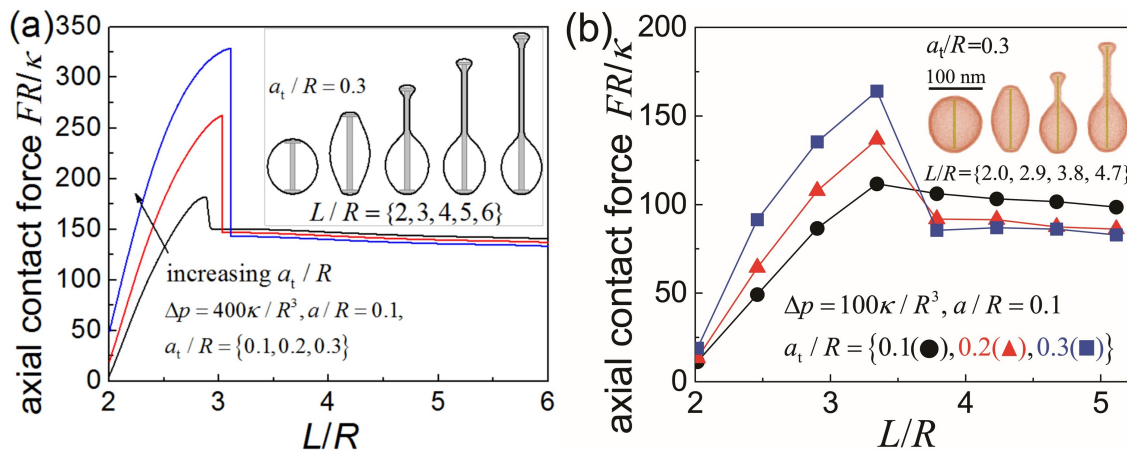
Fig. 5 Normalized axial contact force FR/κ as a function of the normalized nanorod length L/R for $a/R = 0.1$ and different tip sizes $a_t/R = 0.1, 0.2$, and 0.3. (a) Theoretical results at $\Delta p = 400\kappa/R^3$; (b) MD simulations at $\Delta p = 100\kappa/R^3$. Insets plot vesicle morphologies induced by an encapsulated rigid nanorod with radius $a_t/R = 0.3$ at selected lengths.
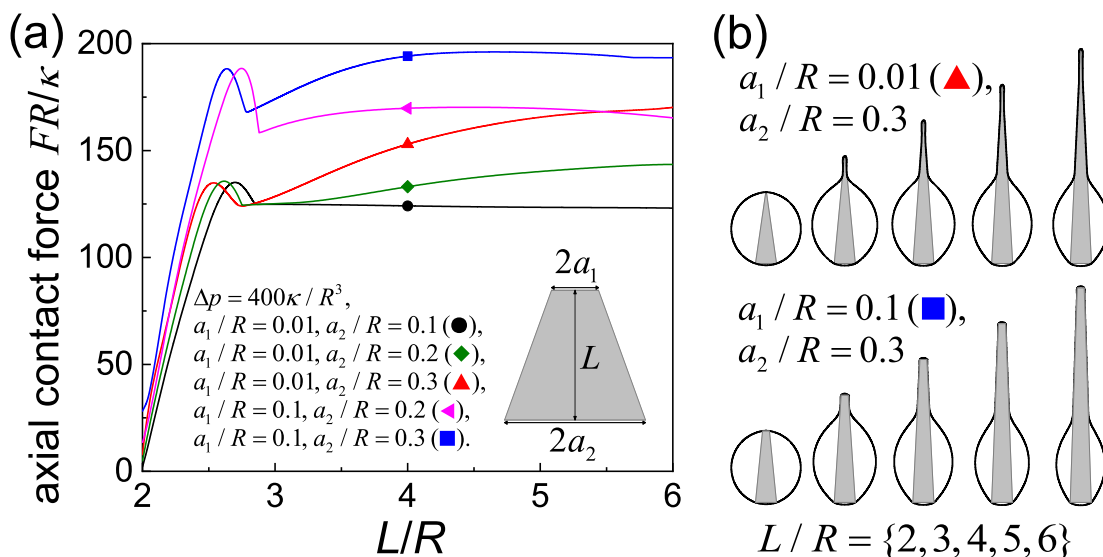

Fig. 6 (a) Normalized axial contact force FR/κ as a function of the normalized nanorod length L/R for $\Delta p = 400\kappa/R^3$ and (b) different geometries of the cone-shaped nanorods. Inset in (a) provides the nanorod geometry with $a_1 < a_2$.

with Fig. 3a). In the case of a large a_2 (e.g., $a_2/R = 0.3$), the force F could reach a higher level than the first peak upon vesicle tubulation. This increase in force can be attributed to a gradual enlargement of membrane tubule in the radial direction (Fig. 6b), as validated by our MD simulations in Fig. S6. In the case of small a_1 and a_2 (e.g., $a_1/R = 0.01$ and $a_2/R = 0.1$), the enlargement of membrane tubule in the radial direction is not evident (Fig. 6b). Therefore, upon vesicle tubulation, the axial contact force and membrane tension exhibit similar linear behaviors with respect to L/R, as in the case of an encapsulated cylindrical nanorod (comparing the black lines in Figs. 6a and S7 with the black lines in Figs. 2 and S2).

4 Discussion

The current results can be used to predict the buckling of a confined elastic rod. We exemplify the encapsulated rod of a uniform radius a as a bundle of weakly cross-linked actin filaments.[49] The critical buckling force for the bundle under simply supported boundary conditions is

$$f_b = \pi^2 \frac{L_p k_B T}{L^2} N,$$

where $L_p = 18$ μm is the persistence length of a single filament,[50] L is the overall length of the filament, and N is the filament number. Here we have assumed that the weakly bundled filaments buckle independently. Thus, f_b is linearly proportional to the filament number N. In the case of a hexagonal

distribution of the filaments in the bundle of radius a, the filament number is around $N = \sqrt{2\pi/3}(3^{3/4} + \sqrt{2\pi}a/d)a/d + 1$, where the distance between neighboring filaments is taken as $d = 20$ nm.[51] The relation between the filament number N and the critical length, at which the encapsulated bundle of actin filaments buckles, can be determined by comparing the critical buckling force f_b and the axial contact forces in Fig. 2.
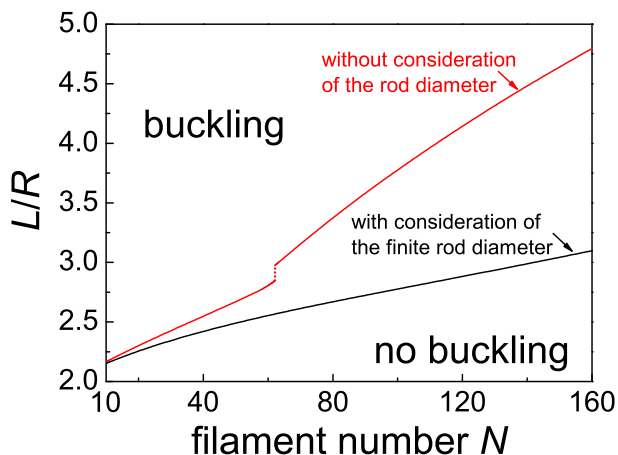

Fig. 7 Buckling phase diagram in terms of the normalized rod length L/R and filament number N at $R = 500$ nm and $\Delta p = 400\kappa/R^3$. The filament bundle of L/R and N above the phase boundary would buckle due to the relatively large axial contact force.

For a vesicle of radius $R = 500$ nm at $\Delta p = 400\kappa/R^3$, a phase diagram on the buckling of an encapsulated cylindrical rod with and without consideration of the finite rod diameter is shown in Fig. 7. In the case where the effect of the rod diameter on the axial contact force is not considered, the vesicle is assumed to form point contact with the filament bundle of radius a and is subjected to a pair of outward point forces. As the force curve at $a/R = 0.01$ in Fig. 2a exhibits an indistinguishable difference from the point force case, it is compared with f_b and a discontinuous phase boundary is determined in which the discontinuity corresponds to the shape transformation of the vesicle before and after tubulation. At small N, no tubulation is formed. As N increases, the vesicle exhibits tubulation. In a more realistic case where the effect of the rod diameter on the force curve is not ignored, the critical length of the filament bundle becomes smaller and this trend becomes more striking as N increases. Moreover, the filament bundle cannot resist the axial force required for vesicle protrusion without buckling in our case study. Here we consider the case $\Delta p = 400\kappa/R^3$. As Δp decreases, the phase boundaries before and after vesicle tubulation move upward and downward, respectively, as the axial contact force decreases at a lower Δp. As demonstrated in Fig. 7, the finite rod diameter is significantly important in regulating the buckling and protrusion of the confined filament bundle.

For a screwdriver-shaped nanorod with two cylindrical portions of different diameters, both curves of F and σ exhibit two local maxima from the theoretical analysis (Fig. S8). The first local maximum located at a relatively small L/R is due to the formation of a tubular membrane protrusion enclosing the upper portion of the nanorod with a smaller diameter, and the second maximum located at a relatively large L/R is due to the growing protrusion enclosing the lower portion of the nanorod with a larger diameter (Fig. S8b).

In addition to the cherry- or bowling pin-like shape, a vesicle encapsulating a long and rigid nanofiber could also resemble the Greek letter ϕ with a pair of tubular membrane protrusions.[3] Experiments, theoretical analysis, and MD simulations indicate that the ϕ-shaped vesicle with vertical symmetry has a slightly higher elastic energy than the cherry-shaped vesicle.[1,12,14] Further experimental studies show that the effective adhesive interaction, such as the binding or friction between the lipid membrane and the enclosed portion of the nanofiber, could facilitate the formation of a ϕ shaped vesicle.[2] In the current study, as the adhesive interaction between the nanofiber and vesicle membrane is neglected, the ϕ-shaped vesicle has not been observed. An interesting question worth further investigation is whether a cherry- or bowling pin-shaped vesicle encapsulating a nanorod is still in a more energetically stable state than a ϕ-shaped vesicle with two tubular protrusions in the presence of adhesive interaction between the nanorod and vesicle membrane. The adhesive interaction not only stabilizes the membrane protrusion but also plays a key role in cell spreading which is guided by the interfacial stiffness of the substrate surface.[52]

The forms of vesicle tubulation analyzed here have also been observed in certain organelles subject to external forces arising from the collective motion of motor proteins along microtubules.[20,21] For example, kinesin motors have been found to pull membrane tubular structures out of giant unilamellar lipid vesicles in vitro[20] and out of autophagosomes, a type of degradative compartment formed by the fusion of autophagosomes and lysosomes during autophagy in vivo.[53] A key difference between the vesicle tubulation induced by a local pulling force and that induced by an encapsulated nanorod of a finite radius a is the presence of contact between the nanorod wall and vesicle membrane. A free tubular membrane structure with bending stiffness κ and membrane tension σ adopts a cylindrical structure of a uniform radius $r_0 = \sqrt{\kappa/(2\sigma)}$ based on the minimization of elastic energy $E = 2\pi r L[\kappa/(2r^2) + \sigma]$ with respect to r.[46,47] In the case of a confined nanorod of radius $a > r_0$, contact between the nanorod wall and vesicle membrane serves as a physical constraint to prevent shrinking of the membrane tubular protrusion from radius a to r_0. From the point of view associated with membrane contact, another case similar to the vesicle tubulation induced by a thick encapsulated nanorod is the vesicle tubulation induced by an aspiration pipette at a large pipette aspiration pressure, where tight contact between the external surface of the vesicle tubule and the internal surface of the pipette could be formed.

From a mechanical point of view, a nuclear envelope can

be modeled as a vesicle with a double lipid bilayer.[9,54] In fission yeast cells, such as *Schizosaccharomyces pombe*, the elongation of spindle microtubules inside a nucleus lacking spindle pole bodies could lead to an abnormal transformation in the shape of the nuclear envelope from a spherical shape to a cherry- or ϕ-like shape.[7–9,54,55] For example, the overexpression of the Mia1p or ned1 gene leads to the formation of acentrosomal microtubule bundles within the nucleus,[7,8] whose elongation further results in tubulation of the nuclear envelope during mitosis or interphase, a stage before mitosis in which cells replicate their chromosomes and synthesize substances for cell division. Similar protrusions of nuclear envelopes have been observed in msd1-null mutant cells, in which anchoring of the microtubules to the spindle pole bodies is impaired.[55] Moreover, the use of microtubule-depolymerizing agents could suppress nuclear protrusions.[54] During anaphase in normal mitotic cell division, sister chromatids separate and move to opposite poles of the cell. The sister chromatids at the cell poles connected by microtubule bundles could be approximated as wide elastic tips to characterize the transformation of the shape of the nuclear envelope. Considering the force distribution on the chromatids[9] and their elastic deformation, our model on the interaction between the vesicle and a nanorod with two widened tips could be generalized to analyze the division of the nuclear envelope.

Our previous work on the pathogenicity of carbon nanotubes within lysosomes indicates that the lysosomal confinement on long and stiff carbon nanotubes leads to local membrane damage due to persistent axial contact between the nanotube and the inner membrane leaflet, causing lipid extraction, lysosomal permeabilization, cathepsin B release into the cytoplasm, and cell death.[12] Moreover, MD simulations show that the critical condition for inducing lysosomal permeabilization can be expressed as a power-law relation between the axial contact force and critical damage time; the lower the contact force, the longer it takes for the membrane damage to occur.[12] Our present work shows that the axial contact force depends not only on the nanotube length but also on its diameter. The larger the nanotube diameter or tip, the higher the maximum axial contact force. Based on our previous analysis,[12] it can be predicted that at the same length, thicker nanorods and nanorods with wider tips could induce membrane damage in a shorter time and thus lysosomal membrane permeabilization, leading to pathogenicity. In the case of a screwdriver-shaped nanorod within a vesicle, the axial contact force curve exhibits two local maxima, and there are more edges of tight contact than in the case of a cylindrical nanorod (Figs. S8 and S9). As membrane damage due to lipid extraction occurs more easily at edges of contact between the carbon nanotube and intracellular membrane,[12] we expect that encapsulated screwdriver-shaped nanotubes with more sharp edges might induce more severe lysosomal damage and consequently more cathepsin B release, initiating a proteolytic cascade culminating in the activation of caspases and leading to cell death by apoptosis.[56]

5   Conclusions

In summary, we present in this paper a theoretical study and molecular dynamics simulations to probe the mechanical interplay between a vesicle and an encapsulated rigid nanorod of finite and non-uniform diameter. Four distinct nanorod shapes are considered: a cylindrical nanorod, a nanorod with two wide ends, a cone-shaped nanorod, and a screwdriver-shaped nanorod. As the nanorod length increases, the vesicle encapsulating a uniform cylindrical nanorod transforms from an initial sphere to a lemon- or conga drum-like shape with vertical symmetry, and then to a cherry- or bowling pin-like shape with a single long, tubular membrane protrusion and a bulge. For a thick and long nanorod, the vesicle evolves from a bowling pin-like shape to a rod-like shape with vertical symmetry. Accompanying the vesicle shape transformation, the axial contact force exerted by the confining vesicle gradually rises to a peak as the nanorod length increases, and then decreases almost linearly with respect to the nanorod length upon vesicle tubulation. The thicker the nanorod, the higher the force peak. Similar features are present in the membrane tension curves. In the case of a cylindrical nanorod with two widened ends, the axial contact force peak becomes proportional to the size of the nanorod tip and is followed by a sharp, discontinuous drop to a constant upon a discontinuous vesicle tubulation evolving from a conga drum-like shape. For a cone-shaped nanorod, vesicle tubulation occurs at the end of the nanorod with a smaller size, with which a smaller axial contact force is associated. After an immediate force drop upon vesicle tubulation, the axial contact force exerted on the cone-shaped nanorod could increase again as the nanorod length increases. The vesicle encapsulating a screwdriver-shaped nanorod is subjected to two peaks of axial contact force due to the formation of a tubular membrane protrusion enclosing the upper and lower nanorod portions of different diameters. Our analysis provides mechanistic insights into the importance of nanorod size and shape for regulating the mechanical interplay between cellular vesicles and encapsulated nanorods, which can serve as a theoretical basis to understand the cellular packing of actin or microtubule bundles,[4,53] filopodial protrusions,[6] and mitotic cell division involving microtubule rearrangement.[7–9,54,55] Recalling that the enforced mechanical contact between carbon nanotubes and intracellular vesicles plays a key role in identifying the membrane damage and pathogenicity of one-dimensional carbon-based materials,[12] our results predict that stiff carbon nanotubes with larger diameters, wider tips, or more edges could aggravate pathogenicity.

putation and Visualization (CCV) at Brown University.

References

1 T. Umeda, H. Nakajima and H. Hotani, *J. Phys. Soc. Jpn.*, 1998, **67**, 682–688.

2 T. Kaneko, T. J. Itoh and H. Hotani, *J. Mol. Biol.*, 1998, **284**, 1671–1681.

3 V. Emsellem, O. Cardoso and P. Tabeling, *Phys. Rev. E: Stat. Phys., Plasmas, Fluids, Relat. Interdiscip. Top.*, 1998, **58**, 4807–4810.

4 F. C. Tsai and G. H. Koenderink, *Soft Matter*, 2015, **11**, 8834–8847.

5 B. Diagouraga, A. Grichine, A. Fertin, J. Wang, S. Khochbin and K. Sadoul, *J. Cell Biol.*, 2014, **204**, 177–185.

6 A. P. Liu, D. L. Richmond, L. Maibaum, S. Pronk, P. L. Geissler and D. A. Fletcher, *Nat. Phys.*, 2008, **4**, 789–793.

7 H. W. G. Lim, G. Huber, Y. Torii, A. Hirata, J. Miller and S. Sazer, *PLoS ONE*, 2007, **2**, e948.

8 L. Zheng, C. Schwartz, V. Magidson, A. Khodjakov and S. Oliferenko, *PLoS Biol.*, 2007, **5**, e170.

9 Q. Zhu, F. Zheng, A. P. Liu, J. Qian, C. Fu and Y. Lin, *Biophys. J.*, 2016, **111**, 2309–2316.

10 C. A. Poland, R. Duffin, I. Kinloch, A. Maynard, W. A. H. Wallace, A. Seaton, V. Stone, S. Brown, W. MacNee and K. Donaldson, *Nat. Nanotechnol.*, 2008, **3**, 423–428.

11 K. Donaldson, R. Aitken, L. Tran, V. Stone, R. Duffin, G. Forrest and A. Alexander, *Toxicol. Sci.*, 2006, **92**, 5–22.

12 W. Zhu, A. von dem Bussche, X. Yi, Y. Qiu, Z. Wang, P. Weston, R. H. Hurt, A. B. Kane and H. Gao, *Proc. Natl. Acad. Sci. U. S. A.*, 2016, **113**, 12374–12379.

13 D. K. Fygenson, M. Elbaum, B. Shraiman and A. Libchaber, *Phys. Rev. E: Stat. Phys., Plasmas, Fluids, Relat. Interdiscip. Top.*, 1997, **55**, 850–859.

14 G. Zou, X. Yi, W. Zhu and H. Gao, *Extreme Mech. Lett.*, 2018, **19**, 20–26.

15 X. Wang, et al., *Nano Lett.*, 2012, **12**, 3050–3061.

16 W. T. Góźdź, *J. Phys. Chem. B*, 2005, **109**, 21145–21149.

17 B. Božič, S. Svetina and B. Žekš, *Phys. Rev. E: Stat. Phys., Plasmas, Fluids, Relat. Interdiscip. Top.*, 1997, **55**, 5834–5842.

18 G. Koster, A. Cacciuto, I. Derényi, D. Frenkel and M. Dogterom, *Phys. Rev. Lett.*, 2005, **94**, 068101.

19 F. Tian, T. Yue, W. Dong, X. Yi and X. Zhang, *Phys. Chem. Chem. Phys.*, 2018, **20**, 3474–3483.

20 C. Leduc, O. Campàs, K. B. Zeldovich, A. Roux, P. Jolimaitre, L. Bourel-Bonnet, B. Goud, J.-F. Joanny, P. Bassereau and J. Prost, *Proc. Natl. Acad. Sci. U. S. A.*, 2004, **101**, 17096–17101.

21 C. Leduc, O. Campàs, J.-F. Joanny, J. Prost and P. Bassereau, *Biochim. Biophys. Acta*, 2010, **1798**, 1418–1426.

22 C. Wang, C. Xu, H. Zeng and S. Sun, *Adv. Mater.*, 2009, **21**, 3045–3052.

23 H.-Q. Wen, H.-Y. Peng, K. Liu, M.-H. Bian, Y.-J. Xu, L. Dong, X. Yan, W.-P. Xu, J.-L. Shen, Y. Lu and H.-S. Qian, *ACS Appl. Mater. Interfaces*, 2017, **9**, 9226–9232.

24 B. Hou, B. Zheng, W. Yang, C. Dong, H. Wang and J. Chang, *J. Colloid Interface Sci.*, 2017, **494**, 363–372.

25 K. Ajima, T. Murakami, Y. Mizoguchi, K. Tsuchida, T. Ichihashi, S. Iijima and M. Yudasaka, *ACS Nano*, 2008, **2**, 2057–2064.

26 M. Zhang, T. Murakami, K. Ajima, K. Tsuchida, A. S. D. Sandanayaka, O. Ito, S. Iijima and M. Yudasaka, *Proc. Natl. Acad. Sci. U. S. A.*, 2008, **105**, 14773–14778.

27 J. Miyawaki, M. Yudasaka, T. Azami, Y. Kubo and S. Iijima, *ACS Nano*, 2008, **2**, 213–226.

28 Y. Tahara, M. Nakamura, M. Yang, M. Zhang, S. Iijima and M. Yudasaka, *Biomaterials*, 2012, **33**, 2762–2769.

29 M. Yang, M. Zhang, Y. Tahara, S. Chechetka, E. Miyako, S. Iijima and M. Yudasaka, *Toxicol. Appl. Pharmacol.*, 2014, **280**, 117–126.

30 W. Z. Helfrich, *Naturforsch. C*, 1973, **28**, 693–703.

31 X. Yi, X. Shi and H. Gao, *Nano Lett.*, 2014, **14**, 1049–1055.

32 J. Nocedal and S. J. Wright, *Numerical Optimization*, 2nd ed. (Springer, New York, 2006).

33 I. R. Cooke and M. Deserno, *J. Chem. Phys.*, 2005, **123**, 224710.

34 B. J. Reynwar, G. Illya, V. A. Harmandaris, M. M. Müller, K. Kremer and M. Deserno, *Nature*, 2007, **447**, 461–464.

35 V. A. Harmandaris and M. Deserno, *J. Chem. Phys.*, 2006, **125**, 204905.

36 M. Laradji and P. B. S. Kumar, *Phys. Rev. Lett.*, 2004, **93**, 198105.

37 K. Yang and Y.-Q. Ma, *Nat. Nanotechnol.*, 2010, **5**, 579–583.

38 T. Yue and X. Zhang, *ACS Nano*, 2012, **6**, 3196–3205.

39 Y. Li, M Kröger and W. K. Liu, *Nanoscale*, 2015, **7**, 16631–16646.

40 S. Plimpton, *J. Comput. Phys.*, 1995, **117**, 1–19.

41 S. Nosé, *J. Chem. Phys.*, 1984, **81**, 511–519.

42 W. G. Hoover, *Phys. Rev. A*, 1985, **31**, 1695–1697.

43 Z. Yang, Y. Zhang, Y. Yang, L. Sun, D. Han, H. Li and C. Wang, *Nanomedicine: Nanotechnol., Biol., Med.*, 2010, **6**, 427–441.

44 X. Xue, L.-R. Wang, Y. Sato, Y. Jiang, M. Berg, D.-S. Yang, R. A. Nixon and X.-J. Liang, *Nano Lett.*, 2014, **14**, 5110–5117.

45 B. Božič, V. Heinrich, S. Svetina and B. Žekš, *Eur. Phys. J. E*, 2001, **6**, 91–98.

46 I. Derényi, F. Jülicher and J. Prost, *Phys. Rev. Lett.*, 2002, **88**, 238101.

47 T. R. Powers, G. Huber and R. E. Goldstein, *Phys. Rev. E: Stat. Phys., Plasmas, Fluids, Relat. Interdiscip. Top.*, 2002, **65**, 041901.

48 B. Pontes, N. B. Viana, L. T. Salgado, M. Farina, V. M. Neto and H. M. Nussenzveig, *Biophys. J.*, 2011, **101**, 43–52.

49 A. Mogilner and B. Rubinstein, *Biophys. J.*, 2005, **89**, 782–795.

50 H. Isambert, P. Venier, A. C. Maggs, A. Fattoum, R. Kassab, D. Pantaloni and M. F. Carlier, *J. Biol. Chem.*, 1995, **270**, 11437–11444.

51 J. C. Adams, *Curr. Opin. Cell Biol.*, 2004, **16**, 590–596.

52 J. Li, D. Han and Y.-P. Zhao, *Sci. Rep.*, 2014, **4**, 3910.

53 Q. P. Su, W. Du, Q. Ji, B. Xue, D. Jiang, Y. Zhu, J. Lou, L. Yu and Y. Sun, *Sci. Rep.*, 2016, **6**, 24002.

54 S. Castagnetti, B. Božič and S. Svetina, *Phys. Chem. Chem. Phys.*, 2015, **17**, 15629–15636.

55 M. Toya, M. Sato, U. Haselmann, K. Asakawa, D. Brunner, C. Antony and T. Toda, *Nat. Cell Biol.*, 2007, **9**, 646–653.

56 J. J. Jr. Reiners, J. A. Caruso, P. Mathieu, B. Chelladurai, X. M. Yin and D. Kessel, *Cell Death Differ.*, 2002, **9**, 934–944.